VIP Photosystem II

DOI: 10.1002/anie.201204705

Two Interconvertible Structures that Explain the Spectroscopic Properties of the Oxygen-Evolving Complex of Photosystem II in the S_2 State**

Dimitrios A. Pantazis, William Ames, Nicholas Cox, Wolfgang Lubitz, and Frank Neese**

Nature's water oxidizing catalyst, the oxygen evolving complex (OEC) of photosystem II (PSII), generates protons, electrons, and molecular oxygen from water and solar energy. During oxygen evolution, the OEC passes through five intermediate states of the so-called Kok or S_i-state cycle,[1] where i denotes the number of stored oxidizing equivalents ($i = 0$–4). O_2 is spontaneously released upon formation of S_4, which then decays back to S_0. Of these states, the most studied intermediate is the S_2 state, which typically exhibits an electron paramagnetic resonance (EPR) multiline signal (MLS) at approximately $g = 2.0$, indicative of a spin $S = 1/2$ ground state.[2] In addition to the $g = 2.0$ MLS, higher spin signals at $g \geq 4.1$ are also observed under a variety of preparation conditions.[3] These signals arise from configurations of the OEC of higher spin multiplicity ($S \geq 5/2$) and represent ground electronic configurations as opposed to sublevels of the same spin manifold which would also include the MLS. Importantly, the two forms of S_2 can be interconverted by near-infrared illumination at cryogenic temperatures.[3c–e]

A rationalization of the phenomena described above is crucial for understanding not only the magnetism and structure–property relationships of the OEC, but also for elucidating the mechanistic details of water splitting on a spectroscopically verified structural basis. Herein we build upon the results of the latest X-ray study on PSII[4] and employ quantum chemical and theoretical spectroscopic techniques to show that the two basic EPR signals of the S_2 state, $g = 2.0$ MLS and the $g \geq 4.1$ signals, arise from two energetically similar and interconvertible structures.

A series of X-ray diffraction (XRD)[5] and X-ray absorption fine structure (EXAFS)[6] studies during the last decade have provided important information about the structure of the OEC and its immediate environment.[7] Following the 1.9 Å resolution XRD structure of PSII by Umena et al.,[4] the inorganic Mn_4O_5Ca core of the OEC and its protein environment can be considered well-defined. The proposed connectivity within the core by Umena et al. was that of a chair-like form containing a distorted Mn_3O_4Ca cubane, with the fourth Mn attached by both a cubane oxo and an additional μ-oxo bridge. The XRD structure was assumed to correspond to the dark-stable S_1 state of the OEC, in which the generally accepted Mn formal oxidation states are $Mn^{III}{}_2Mn^{IV}{}_2$. However, more recent studies[7,8] have provided strong evidence that the inorganic core was modified by radiation-induced Mn reduction. This is in line with the expected reduction of a percentage of Mn ions to the +2 oxidation state based on the reported X-ray dose.[9] Although much better controlled than in previous XRD models, this perturbation is still apparent when considering the surprisingly long Mn–O bond distances, which are chemically unreasonable for $Mn^{III/IV}$ oxidation states,[10] as well as the odd nonbonding position of a putative μ_4-oxo bridge (O5). This particular feature would give rise to significant spin density on O5 (Supporting Information, Figure S1), which would be inconsistent with experiment.[8b] Recent studies by Luber et al.[8a] suggest that the 1.9 Å XRD Mn_4O_5Ca core is representative not of S_1 but of a mixture of reduced forms beyond the physiological states of the Kok cycle, while Dau[7] and Knapp[8c] have concluded that this XRD model is mostly representative of the reduced S_{-3} state.

Despite this problem, the 1.9 Å XRD structure remains the best starting point for developing models that attempt to establish connections between structural features and spectroscopic observables. In the present work, the XRD structure is used to construct large 238-atom cluster models of the OEC (Figure 1). Their structures were optimized and their proper-

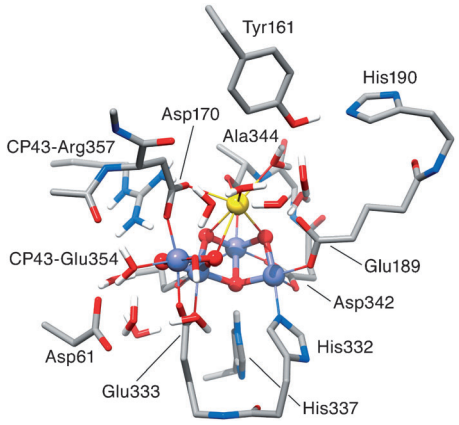

Figure 1. The 238-atom OEC cluster model (core structure **A** shown) used in the present work. H white, C gray, N blue, O red, Mn purple, Ca yellow. Most hydrogen atoms have been omitted for clarity.

[*] Dr. D. A. Pantazis, Dr. W. Ames, Dr. N. Cox, Prof. Dr. W. Lubitz, Prof. Dr. F. Neese
Max Planck Institute for Chemical Energy Conversion
Stiftstrasse 34–36, 45470 Mülheim an der Ruhr (Germany)
E-mail: dimitrios.pantazis@cec.mpg.de
frank.neese@cec.mpg.de

[**] We thank the MPG for financial support.

Supporting information for this article is available on the WWW under http://dx.doi.org/10.1002/anie.201204705.

ties were computed for the spectroscopically well-characterized S_2 state ($Mn^{III}Mn^{IV}_3$) of the Kok cycle. The models contain the seven directly-coordinating amino acids (all from chain D1 unless otherwise indicated): Asp170, Glu189, His332, Glu333, Asp342, Ala344, and CP43-Glu354, as well as two H_2O molecules on Ca^{2+} and an H_2O plus a hydroxide on a terminal Mn (Mn4, following the XRD labeling). Additionally, the models contain the Asp61, Tyr161 (Y_Z), His190, and His337 residues because they form H-bonds with the Mn-bound ligands (Asp61), the Ca-bound and vicinal water molecules (Tyr161 and His190), and the O3 bridge of the cluster (His337). CP43-Arg357 is also included because its positively charged side chain provides an important second-sphere interaction with the cluster. Eight closely associated crystallographic water molecules are also included, while the backbone of Leu343 and partial backbones of Ser169 and Gly171 are incorporated as structural directing agents for the non-coordinating waters. Protonation states follow the pattern previously determined from comparison of computed ^{55}Mn hyperfine coupling constants (HFCs) with experiment.[8b] Appropriate backbone constraints were imposed to ensure that the structural effects of the protein environment are taken into account.[11]

Many optimization trajectories using dispersion-corrected[12] scalar relativistic[13] density functional theory with all-electron basis sets,[14] as implemented in the ORCA program,[15] were followed (see Supporting Information for details). These varied in the starting positions of the Mn_4O_5Ca ions and of the ligating residues to ensure that the conformational space was adequately sampled. All calculations invariably converged to one of two almost isoenergetic structures **A** and **B**, which share the same coordination environment (Figure 1) but differ fundamentally in the bonding within the inorganic core (Figure 2). Structures **A** and **B** have localized

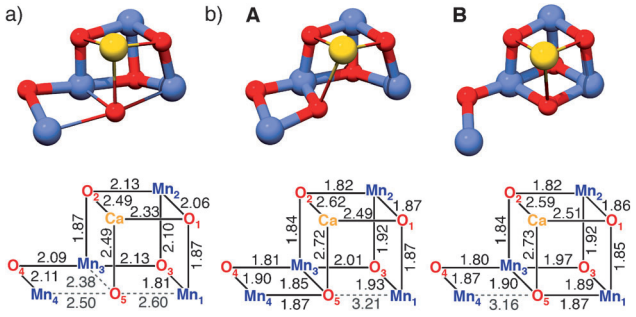

Figure 2. Mn_4O_5Ca cores and metal–oxygen distances [Å] from a) the 1.9 Å XRD structure and b) the optimized S_2 state models **A** and **B**.

Mn valencies (Supporting Information, Table S1), with the unique Mn^{III} ion at opposite centers of the cluster. They differ from the XRD mostly in the Mn–Mn connectivity imposed by the position of the O5 bridge; as shown below, this has profound implications for the electronic structure and the expected spectroscopic properties of the OEC.

In terms of relative energies, model **A** is consistently predicted to be more stable by a small margin of the order of 1 kcal mol^{-1}. This energy difference is not very sensitive with respect to the density functional used, although it is somewhat affected by dispersion corrections (see the Supporting Information, Table S2 for a comparison of methods). The intrinsic limitations in the accuracy of DFT and the approximations involved in constructing and treating the present models, such as the neglect of dynamics and of the protein environment further from the OEC, imply that quantitative uncertainty estimates are unattainable. Nevertheless, the fairly stable predictions obtained by different functionals strongly suggest that both structural forms should be observable.

Successive calculations within the relaxed protein pocket comparing the XRD Mn_4O_5Ca core with the optimized S_2 state cores show that the optimized forms are stabilized by about 107 kcal mol^{-1}. Only about one fifth of the stabilization is due to changes in Mn positions, which decrease slightly and move towards better agreement with EXAFS measurements[6a] (Table 1). Instead, the largest stabilization (86 kcal mol^{-1}) arises from the optimization of the oxo bridges (Figure 2) and over half of that (46 kcal mol^{-1}) from the shift of the quasi radical O5 towards chemically proper bonding distance with either of the two terminal Mn ions, Mn1 or Mn4. Structure **A** is obtained if O5 binds to Mn4: in this case, the cubane part is opened and Mn1 remains pentacoordinate as the unique Mn^{III} site of the S_2 state. This type of structure is the one lower in energy and essentially coincides with a model of the OEC originally proposed by Siegbahn,[16] and it is already confirmed as spectroscopically valid.[2k] Mechanistic studies by Siegbahn additionally suggested that this might represent the catalytically active form.[16] In the alternative structure **B**, a chemically proper Mn_3O_4Ca cuboid is formed and the dangling Mn4 becomes instead the pentacoordinate Mn^{III} site. Structure **B** is very similar to a model proposed by Barber and Murray[17] as a revision of the original "London" XRD structure.[5c]

Table 1: Comparison of metal–metal distances [Å] between models **A** and **B**, the 1.9 Å XRD structure, and EXAFS.

	A	B	XRD[a]	EXAFS
Mn1–Mn2	2.81	2.75	2.84/2.76	
Mn1–Mn3	3.38	2.89	3.29/3.30	2.7, 2.8, 3.3
Mn2–Mn3	2.80	2.76	2.89/2.91	(2:1:1)
Mn3–Mn4	2.76	3.13	2.97/2.91	
Mn1–Ca	3.70	3.48	3.51/3.46	
Mn2–Ca	3.43	3.48	3.36/3.29	3.4, 3.9
Mn3–Ca	3.58	3.52	3.41/3.44	(2:2 or 3:1)
Mn4–Ca	3.99	4.17	3.79/3.80	

[a] Values from chains A/a of the PSII dimer.

The exchange coupling constants J_{ij} of the two structures (Figure 3) were calculated using the broken symmetry approach. All six pairwise J values were extracted from the high-spin and the seven broken-symmetry determinants as described in detail earlier.[18] Using the set of J values derived for each structure, the Heisenberg–Dirac–van Vleck Hamiltonian was subsequently diagonalized to obtain the complete spectrum of 320 magnetic levels that arise from the coupling of the four high-spin Mn ions. Structure **A** has an $S = 1/2$ ground state, while the first excited state ($S = 3/2$) is 23 cm^{-1}

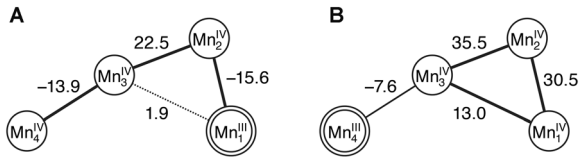

Figure 3. Computed nearest-neighbor exchange coupling constants [cm^{-1}] and distribution of Mn oxidation states for models **A** and **B**.

higher, which is similar to previously studied models and in agreement with experiment on the MLS signal of the S_2 state. Additionally, the calculated isotropic ^{55}Mn HFCs (−212, 201, 176, and −280 MHz for Mn1–Mn4, respectively) agree well with those published previously for this type of model, and with experiment.[2f,k] For an EPR simulation based on the DFT calculated parameters that includes hyperfine and *g*-anisotropy, see Figure 4.

The defining feature of structure **B** is the ferromagnetic coupling between the three Mn^{IV} ions of the Mn_3Ca cubane unit. The angles formed at the oxo corners of the cubane inhibit any antiferromagnetic exchange interactions,[19] making the Mn_3Ca cubane an intrinsically high-spin $S = 9/2$ unit. A most compelling confirmation of the present observations comes from a recent characterization of a synthetic $Mn^{IV}{}_3O_4Ca$ cubane by Christou and co-workers.[20] Magnetic susceptibility studies established a ground state of $S = 9/2$ for this compound, owing to the dominant ferromagnetic coupling between the Mn pairs. Calculations in our laboratory accurately reproduce the experimental data for this complex and suggest that the same situation holds for the other existing synthetic $Mn^{IV}{}_3O_4Ca$ cubane reported by Agapie and co-workers.[21]

The total spin in the case of model **B** is thus regulated by the balance of the ferromagnetic interactions in the cubane and the unique antiferromagnetic coupling between the μ-oxo bridged Mn3 and Mn4 ($J_{34} = -7.6\ cm^{-1}$). Here the magnetic interactions result in a total spin 5/2 ground state with a close-lying $S = 7/2$ excited state, in agreement with the expected spin of the high-spin species that gives rise to the $g \geq 4.1$ signals. If typical *g* and fine structure values for the Mn^{III} ($g = 2$, $d = -1$ to $-6\ cm^{-1}$) and Mn^{IV} ($g = 2$, $d = 0\ cm^{-1}$) ions are assumed, the calculated spin ladder yields a broad X-band EPR spectrum, with low-field turning points in the $g = 4$–10 region (see Supporting Information for more details). The lineshape is similar to the high spin signals seen in *T. elongatus* and higher plant PSII, which are generated by infrared light excitation of the S_2 MLS state at cryogenic (> 65 K) temperatures.[3d] Spectral lines appear distant from $g = 2.0$ (weak-field limit) as the total zero-field splitting of the ground state spin sub-manifold is larger than the resonance condition/microwave quantum ($D > h\nu$; see Figure 4). Of additional note is that the calculated HFCs for model **B** yield an average projected hyperfine spacing of 87 MHz (31 G), which is approximately the same as observed for the $g = 4.1$ signal seen in higher plants treated with NH_3.[22] This splitting is of similar magnitude to that measured for Christou's $Mn^{IV}{}_3O_4Ca$ complex; isotropic on-site HFCs of −150 MHz to −180 MHz were computed for model **B** as compared to −180 MHz for the synthetic $Mn^{IV}{}_3O_4Ca$ compound.[20]

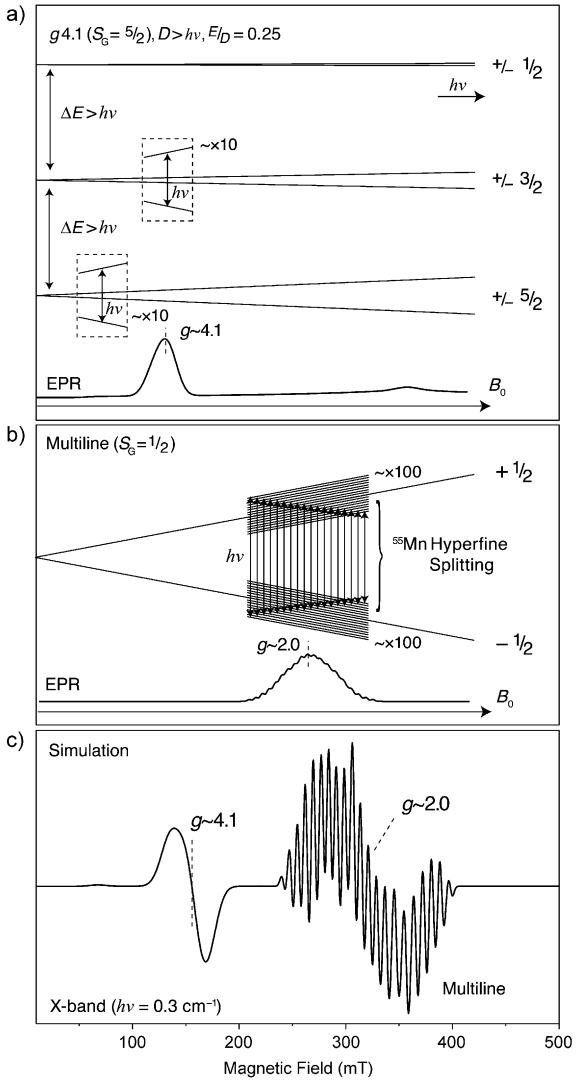

Figure 4. X-Band (9 GHz) EPR simulations of the two electronic configurations of the S_2 state using the DFT-derived parameters listed in the Supporting Information, Table S3. a) Energy levels of the $S_T(GS) = 5/2$ ($g \approx 4.1$) configuration and corresponding powder EPR simulation. A value of $D = 0.59\ cm^{-1}$ is assumed, which corresponds to an on-site fine structure value of 3 cm^{-1} for Mn^{III}. The dominant narrow feature of the EPR spectrum observed at $g \approx 4.1$ originates from the spin-allowed transition between the levels of the $\pm 3/2$ Kramers doublet; the $\pm 3/2$ transition occurs at approximately the same *g* position for all powder orientations. b) Energy levels of the $S_T(GS) = 1/2$ (MLS) configuration and corresponding powder pattern EPR simulation. c) First-derivative EPR simulation of both the MLS and $g \approx 4.1$ configurations.

The energy ladder for model **B** is quite compressed compared to model **A**, resulting in very small energy separations between the ground and first excited states. This in turn renders the energy gap sensitive to perturbations, such as reorganization of the hydrogen-bonding network involving different proton orientations of ligated OH^-/H_2O ligands and/or proximal water molecules. Indeed, even different computational treatments are sufficient to perturb this energy gap at least within the range 1–6 cm^{-1} for model **B**. This behavior mirrors what is experimentally observed. The nature of the

$g \geq 4.1$ signals of higher plants, generated by near infrared excitation of the MLS, varies depending on illumination temperature. At low temperatures, high g signals (5–9) are favored, whereas at 100–150 K a signal is observed at $g \approx 4.1$. High g signals can be converted to the $g \approx 4.1$ signal simply by annealing to 150 K. This phenomenology has been interpreted as evidence for at least two high spin $S = 5/2$ configurations that differ in terms of the total ZFS of the ground state manifold. A change in the ZFS could be caused by either: 1) a change in the on-site Mn fine structure values, which is unlikely as the Mn ions do not change their ligand environment or oxidation state (assuming both high g states represent model **B**); or 2) a change in the ladder spacing (energy gap) of the spin submanifolds, as described above. An increase/decrease of the energy spacing leads to expansion/contraction of the whole energy ladder, which in effect changes the ZFS of the ground state manifold.

Indeed, for a spin ladder where the energy spacing between the ground and first excited state is of the order of 10 cm^{-1}, the ground state cannot be considered well-isolated, and thus broad EPR signals of significant complexity are expected even when the on-site fine structure terms are large ($d \gg h\nu$; Supporting Information, Figures S3–S5). It is this condition that results in the high g signals observed in both higher plants and cyanobacteria. In contrast, for a spin ladder where the energy ladder spacing is large (of the order of 100 cm^{-1}), the complexity of the $g \geq 4.1$ signal is lost. In this case, the ZFS of the ground state manifold is well-defined, and only a single EPR turning point is observed that is centered at $g \approx 4.1$ (at X-band frequencies). Within the assumption that the ground state of the high spin species is well-isolated, a theoretical estimate of the ZFS of the ground state manifold can be made (see Supporting Information). Model **B** predicts a ZFS (D) of -0.2 to -1.2 cm^{-1}. This compares well to the measured estimate, that is, $|D| \approx 0.5$ cm^{-1}.

There is evidence that at cryogenic temperatures, electron-coupled proton transfer events can decouple. A good example of this is the photoinduced oxidation of the redox-active tyrosine (Y_D) residue of PSII.[23] When formed at liquid helium temperatures, proton movement to the nearby histidine residue acting as a base is inhibited. The proton only translocates upon annealing to 100 K. Thus, the exact protonation state of the high-spin system formed by NIR illumination at 65 K could indeed be different from the same state form at 150 K, leading to the phenomenology described above.

The transition state (TS) for the interconversion between the **A** and **B** cluster models, and thus for the interconversion between the MLS and the $g \geq 4$ signals, was estimated using two approaches. First, relaxed scans along the isomerization coordinate between the models **A** and **B** in step sizes of 0.0625 Å were completed, giving a maximal barrier of 9.0 kcal mol^{-1}. This energy can be considered as an upper bound to the true barrier for **A**–**B** interconversion in the OEC, since the approximate TS is unrelaxed with respect to the TS mode and subject to backbone constraints. The second approach consisted of constructing constrained truncated 120-atom models of **A** and **B**, locating an approximate TS between them with a relaxed scan, and subsequently optimizing the corresponding transition state utilizing the hybrid Hessian feature of ORCA. Locating the TS proved challenging, partly because it involves an interchange of oxidation states between the two terminal Mn ions. The approach that was successful consisted in employing an initial hybrid Hessian of 51 atoms to identify the transition state mode and steer optimization towards the desired saddle point. Full numerical frequencies at the stationary point confirmed that the true transition state was obtained, yielding an imaginary frequency (-141 cm^{-1}) of the correct mode. This TS (Supporting Information, Figure S6) yields a lower estimate for the barrier of 6.4 kcal mol^{-1}. Although methodologically related uncertainties are unavoidable, it can be concluded that the barrier is sufficiently low to allow interconversion of the two structural forms under physiological conditions.

Most importantly, the results show that the coordinate along which the interconversion occurs requires a significant reduction of the Mn1···Mn4 interatomic distance, from approximately 4.7 Å for the truncated models of **A** and **B** to less than 4.2 Å in the transition state. This is the key feature in maintaining a low-energy barrier for the interconversion of the two core structures, as it allows for a smooth valence exchange between the terminal Mn1 and Mn4 ions, which at the TS share the spin that swaps between minima **A** and **B** (computed Mulliken spin populations of 3.42 and 3.46 for Mn1 and Mn4, respectively). At the same time, this TS entirely avoids the development of radical character on O5 (spin population -0.04); as mentioned previously, without such a geometric change the barrier for O5 interconversion could be as high as 46 kcal mol^{-1}, the relaxation energy for the O5 position in the 1.9 Å XRD structure.

The potential for structural fluxionality in manganese oxo clusters has been suggested before from highly simplified models with different stoichiometry and Mn oxidation states than the ones adopted here.[24] Given the more up-to-date XRD information, of greater relevance to the present work is Kusunoki's suggestion that several structures can in principle exist in the S_1 state, which are close in energy and are related by proton migration.[25] The present results, combining refinement of XRD structural models with analysis of their magnetic properties, demonstrate for the first time that two interconvertible structural forms of the OEC core exist in the S_2 state and establish their correspondence with the two observed types of EPR signals. This provides a firm structural basis for rationalizing not only the spectroscopy of the S_2 state, but also most of the related phenomenology that has been observed during the last three decades. For example, as this interconversion involves the oxidation state change of the solvent-accessible Mn4 it is perhaps unsurprising that small molecule additives such as EtOH, MeOH, and NH_3 alter the equilibrium between the MLS and $g \geq 4.1$ states.[2g,j,3a] An atomic-level understanding of such phenomena is now accessible.

In addition to the electronic structure, the results have implications for the substrate exchange and water oxidation mechanisms. Both models are valence-localized, with one empty coordination site that can presumably accommodate an extra water substrate. Thus, the nearly isoenergetic nature

of **B** with respect to **A** implies that the S_2–S_3 transition of the Kok cycle can potentially proceed through more than one pathway. This would be compatible with a recently presented mechanism for the S_2 to S_3 transition[26] that involves an additional H_2O binding at Mn1 of structure **A**, but allows in principle for other possibilities if structure **B** also advances to S_3. The presence of an open coordination site along the Mn^{III} pseudo Jahn–Teller axis in models **A** and **B** is an inescapable result of the optimization of the photoreduced XRD structure and appears as a fundamental structural element of the S_2-state OEC under catalytic temperatures. Coordinatively unsaturated Mn sites have also been identified as prerequisite for catalytic activity in a family of Mn oxides.[27]

In terms of the water-splitting mechanism, the present results provide support for a possible identification of one of the water substrates. It has been previously proposed that the O5 μ-oxo bridge is exchangeable and possibly represents one of the two O atoms forming O_2. The two substrate water molecules of the OEC display very different binding kinetics.[28] The early binding, slow-exchanging substrate (termed W_{slow}) is considered to be associated with the OEC through the S-state cycle and presumably represents an oxygen ligand of the Mn_4O_5Ca cluster. The fast exchanging substrate (W_{fast}) has unresolved binding kinetics prior to S_3, suggesting it is only loosely associated with the OEC prior to O–O bond formation. An important observation for W_{slow} is that it exchanges in all S-states. However, the slowest exchange rate is relatively fast, with a half-time of the order of seconds, whereas all known complexes of high-valent Mn^{III}/Mn^{IV} ions display much slower rates of exchange for μ-oxo bridge(s) with bulk solvent, with half-times of the order of 10^4–10^5 s.[29] Thus, for a μ-oxo bridge to represent a substrate site in S_1/S_2, the OEC must contain a structural element that is not present in these model systems. The present study offers a way to reconcile these conflicting observations by suggesting that the facile interconversion between the two geometric forms, **A** and **B**, by the simple shift of the O5 ligand is an important factor for substrate exchange in the S_2 state. This large molecular motion, which is absent in model dimer systems, may speed up bridge exchange with surrounding OH^-/H_2O ligands or solvent. Experimental and theoretical investigations are ongoing in our laboratory to determine if this is indeed the case.

Received: June 15, 2012
Published online: August 21, 2012

Keywords: density functional calculations · EPR spectroscopy · oxygen evolving complex · photosystem II · water splitting

[1] B. Kok, B. Forbush, M. McGloin, *Photochem. Photobiol.* **1970**, *11*, 457–475.

[2] a) A. Haddy, *Photosynth. Res.* **2007**, *92*, 357–368; b) G. C. Dismukes, Y. Siderer, *Proc. Natl. Acad. Sci. USA* **1981**, *78*, 274–278; c) O. Hansson, L. E. Andreasson, *Biochim. Biophys. Acta Bioenerg.* **1982**, *679*, 261–268; d) J. C. De Paula, G. W. Brudvig, *J. Am. Chem. Soc.* **1985**, *107*, 2643–2648; e) W. F. Beck, J. C. De Paula, G. W. Brudvig, *J. Am. Chem. Soc.* **1986**, *108*, 4018–4022; f) D. W. Randall, B. E. Sturgeon, J. A. Ball, G. A. Lorigan, M. K. Chan, M. P. Klein, W. H. Armstrong, R. D. Britt, *J. Am. Chem. Soc.* **1995**, *117*, 11780–11789; g) J. M. Peloquin, K. A. Campbell, D. W. Randall, M. A. Evanchik, V. L. Pecoraro, W. H. Armstrong, R. D. Britt, *J. Am. Chem. Soc.* **2000**, *122*, 10926–10942; h) M.-F. Charlot, A. Boussac, G. Blondin, *Biochim. Biophys. Acta Bioenerg.* **2005**, *1708*, 120–132; i) L. V. Kulik, B. Epel, W. Lubitz, J. Messinger, *J. Am. Chem. Soc.* **2007**, *129*, 13421–13435; j) J.-H. Su, N. Cox, W. Ames, D. A. Pantazis, L. Rapatskiy, T. Lohmiller, L. V. Kulik, P. Dorlet, A. W. Rutherford, F. Neese, A. Boussac, W. Lubitz, J. Messinger, *Biochim. Biophys. Acta Bioenerg.* **2011**, *1807*, 829–840; k) N. Cox, L. Rapatskiy, J.-H. Su, D. A. Pantazis, M. Sugiura, L. Kulik, P. Dorlet, A. W. Rutherford, F. Neese, A. Boussac, W. Lubitz, J. Messinger, *J. Am. Chem. Soc.* **2011**, *133*, 3635–3648.

[3] a) A. Haddy, K. V. Lakshmi, G. W. Brudvig, H. A. Frank, *Biophys. J.* **2004**, *87*, 2885–2896; b) P. J. Smith, R. J. Pace, *Biochim. Biophys. Acta Bioenerg.* **1996**, *1275*, 213–220; c) A. Boussac, J.-J. Girerd, A. W. Rutherford, *Biochemistry* **1996**, *35*, 6984–6989; d) A. Boussac, S. Un, O. Horner, A. W. Rutherford, *Biochemistry* **1998**, *37*, 4001–4007; e) A. Boussac, H. Kuhl, S. Un, M. Rögner, A. W. Rutherford, *Biochemistry* **1998**, *37*, 8995–9000; f) J. M. Peloquin, R. D. Britt, *Biochim. Biophys. Acta Bioenerg.* **2001**, *1503*, 96–111.

[4] Y. Umena, K. Kawakami, J.-R. Shen, N. Kamiya, *Nature* **2011**, *473*, 55–60.

[5] a) A. Zouni, H. T. Witt, J. Kern, P. Fromme, N. Krauss, W. Saenger, P. Orth, *Nature* **2001**, *409*, 739–743; b) N. Kamiya, J.-R. Shen, *Proc. Natl. Acad. Sci. USA* **2003**, *100*, 98–103; c) K. N. Ferreira, T. M. Iverson, K. Maghlaoui, J. Barber, S. Iwata, *Science* **2004**, *303*, 1831–1838; d) B. Loll, J. Kern, W. Saenger, A. Zouni, J. Biesiadka, *Nature* **2005**, *438*, 1040–1044.

[6] a) Y. Pushkar, J. Yano, K. Sauer, A. Boussac, V. K. Yachandra, *Proc. Natl. Acad. Sci. USA* **2008**, *105*, 1879–1884; b) H. Dau, A. Grundmeier, P. Loja, M. Haumann, *Philos. Trans. R. Soc. London Ser. B* **2008**, *363*, 1237–1243.

[7] A. Grundmeier, H. Dau, *Biochim. Biophys. Acta Bioenerg.* **2012**, *1817*, 88–105.

[8] a) S. Luber, I. Rivalta, Y. Umena, K. Kawakami, J. R. Shen, N. Kamiya, G. W. Brudvig, V. S. Batista, *Biochemistry* **2011**, *50*, 6308–6311; b) W. Ames, D. A. Pantazis, V. Krewald, N. Cox, J. Messinger, W. Lubitz, F. Neese, *J. Am. Chem. Soc.* **2011**, *133*, 19743–19757; c) A. Galstyan, A. Robertazzi, E. W. Knapp, *J. Am. Chem. Soc.* **2012**, *134*, 7442–7449.

[9] J. Yano, J. Kern, K.-D. Irrgang, M. J. Latimer, U. Bergmann, P. Glatzel, Y. Pushkar, J. Biesiadka, B. Loll, K. Sauer, J. Messinger, A. Zouni, V. K. Yachandra, *Proc. Natl. Acad. Sci. USA* **2005**, *102*, 12047–12052.

[10] A. Robertazzi, A. Galstyan, E. W. Knapp, *CrystEngComm* **2011**, *13*, 6369–6372.

[11] P. E. M. Siegbahn, *ChemPhysChem* **2011**, *12*, 3274–3280.

[12] S. Grimme, J. Antony, S. Ehrlich, H. Krieg, *J. Chem. Phys.* **2010**, *132*, 154104–154119.

[13] E. van Lenthe, E. J. Baerends, J. G. Snijders, *J. Chem. Phys.* **1994**, *101*, 9783–9792.

[14] D. A. Pantazis, X. Y. Chen, C. R. Landis, F. Neese, *J. Chem. Theory Comput.* **2008**, *4*, 908–919.

[15] F. Neese, *Wiley Interdiscip. Rev. Comput. Mol. Sci.* **2012**, *2*, 73–78.

[16] a) P. E. M. Siegbahn, *Chem. Eur. J.* **2008**, *14*, 8290–8302; b) P. E. M. Siegbahn, *Acc. Chem. Res.* **2009**, *42*, 1871–1880.

[17] J. Barber, J. W. Murray, *Philos. Trans. R. Soc. London Ser. B* **2008**, *363*, 1129–1137.

[18] a) D. A. Pantazis, M. Orio, T. Petrenko, S. Zein, E. Bill, W. Lubitz, J. Messinger, F. Neese, *Chem. Eur. J.* **2009**, *15*, 5108–5123; b) D. A. Pantazis, M. Orio, T. Petrenko, S. Zein, W. Lubitz, J. Messinger, F. Neese, *Phys. Chem. Chem. Phys.* **2009**, *11*, 6788–6798.

[19] D. A. Pantazis, V. Krewald, M. Orio, F. Neese, *Dalton Trans.* **2010**, *39*, 4959 – 4967.
[20] S. Mukherjee, J. A. Stull, J. Yano, T. C. Stamatatos, K. Pringouri, T. A. Stich, K. A. Abboud, R. D. Britt, V. K. Yachandra, G. Christou, *Proc. Natl. Acad. Sci. USA* **2012**, *109*, 2257 – 2262.
[21] J. S. Kanady, E. Y. Tsui, M. W. Day, T. Agapie, *Science* **2011**, *333*, 733 – 736.
[22] D. H. Kim, R. D. Britt, M. P. Klein, K. Sauer, *J. Am. Chem. Soc.* **1990**, *112*, 9389 – 9391.
[23] P. Faller, C. Goussias, A. W. Rutherford, S. Un, *Proc. Natl. Acad. Sci. USA* **2003**, *100*, 8732 – 8735.
[24] S. Petrie, R. Stranger, P. Gatt, R. J. Pace, *Chem. Eur. J.* **2007**, *13*, 5082 – 5089.
[25] M. Kusunoki, *J. Photochem. Photobiol. B* **2011**, *104*, 100 – 110.
[26] P. E. M. Siegbahn, *Phys. Chem. Chem. Phys.* **2012**, *14*, 4849 – 4856.
[27] I. Zaharieva, M. M. Najafpour, M. Wiechen, M. Haumann, P. Kurz, H. Dau, *Energy Environ. Sci.* **2011**, *4*, 2400 – 2408.
[28] W. Hillier, J. Messinger, T. Wydrzynski, *Biochemistry* **1998**, *37*, 16908 – 16914.
[29] R. Tagore, H. Chen, R. H. Crabtree, G. W. Brudvig, *J. Am. Chem. Soc.* **2006**, *128*, 9457 – 9465.

